

A FRICTIONAL COSSERAT MODEL FOR THE FLOW OF GRANULAR MATERIALS THROUGH A VERTICAL CHANNEL

L. SRINIVASA MOHAN, PRABHU R. NOTT, AND K. KESAVA RAO

Summary. A rigid-plastic Cosserat model has been used to study dense, fully developed flow of granular materials through a vertical channel. Frictional models based on the classical continuum do not predict the occurrence of shear layers, at variance with experimental observations. This feature has been attributed to the absence of a material length scale in their constitutive equations. The present model incorporates such a material length scale by treating the granular material as a Cosserat continuum. Thus localised couple stresses exist and the stress tensor is asymmetric. The velocity profiles predicted by the model are in close agreement with available experimental data. The predicted dependence of the shear layer thickness on the width of the channel is in reasonable agreement with data. In the limit of small ϵ (ratio of the particle diameter to the half-width of the channel), the model predicts that the shear layer thickness scaled by the particle diameter grows as $\epsilon^{-1/3}$.

1. INTRODUCTION

In many terrestrial flows of granular materials, gravity consolidates the medium to a state where sustained frictional contact between the particles is the dominant mode of momentum transfer. In this regime of high solids fraction and low deformation rate, models based on concepts in metal plasticity and soil mechanics have been traditionally used to describe the flow [1]. While many gross features of granular flows can be predicted using these models, one aspect they fail to capture is the thickness of shear layers; often when granular materials are sheared, large portions of the material do not suffer sustained deformation. In the experiments of Roscoe [2], Nedderman and Laohakul [3], Gudehus and Tejchman [4], the velocity gradients are confined to layers approximately 5–40 particle diameters in thickness. Moreover, the thickness of the shear layers is influenced by the nature of the boundaries; when the flowing medium is confined by smooth walls, it is found that the thickness of the shear layers is less than that in the case of rough walls [3, 5].

Conventional models of plasticity do not predict shear layers [6, 7]. The failure of the frictional models to predict the thickness of the shear layers accurately has been attributed to the absence of a material length scale in their constitutive equations [8, cited in 9]. To overcome this deficiency of the classical models, the particle size must be incorporated in the constitutive equations. In the absence of a comprehensive micro-mechanical model to describe friction, a continuum theory that includes a material length scale in the constitutive equations can be constructed by modelling the granular material as a Cosserat continuum [8]. We shall argue later that the frictional nature of particle interactions provides sufficient grounds for using this approach. We note here that models based on kinetic theory [see, for example, 10], involve the particle diameter in the constitutive relations. However,

these models are expected to hold only for rapid flows, where particle interactions may be approximated by instantaneous collisions.

In this paper, we explore the use of a Cosserat plasticity model to describe steady, fully developed, plane flow of a granular material in a vertical channel under the action of gravity. The predictions of the model will be compared with data reported in the literature. While Cosserat plasticity models have been applied to problems in granular flow in the past [5, 6, 9, 11, 12], these studies address unsteady flows and are posed in terms of strain increments; with this formulation, Tejchman and Gudehus [5] found it difficult to integrate the equations numerically for large times. To the best of our knowledge, the present work represents the first attempt to examine steady flow in this context. We indicate below how the model is developed, and then apply it to channel flow.

2. THE COSSERAT MODEL

The field variables of the classical continuum are the density ρ , the linear velocity \underline{v} , and the stress tensor $\underline{\sigma}$. A Cosserat continuum ([13,p. 223]; [14]) involves two additional field variables, namely, the angular velocity $\underline{\omega}$, and the couple stress tensor \underline{M} . Considering a Cartesian coordinate system (figure 1), M_{xz} represents the couple per unit area exerted about the z -axis on a plane $x = \text{constant}$, by the material to the left of this plane. A positive value of M_{xz} is taken to impose an anti-clockwise rotation on this plane (figure 1). For a Cosserat continuum, the mass and linear momentum balances must be supplemented by the angular momentum balance, which relates $\underline{\omega}$, \underline{M} , and $\underline{\sigma}$. For steady, fully developed flow, spatial gradients of \underline{M} cause $\underline{\sigma}$ to be asymmetric. This is in contrast to the classical continuum, which assumes implicitly that there are no couple stresses, body couples, and intrinsic angular momentum; hence the angular momentum balance can be satisfied identically by requiring $\underline{\sigma}$ to be symmetric.

There is enough analytical evidence to motivate the use of a Cosserat model in the present problem. Dahler [15] used a statistical mechanical approach to develop expressions for the stresses in a fluid composed of diatomic molecules. For molecules interacting via central forces, which are directed along the lines joining the centers of mass of the molecules, $\underline{\sigma}$ is found to be symmetric. However, his model suggests that non-central forces may cause $\underline{\sigma}$ to be asymmetric. Campbell [16] simulated the shearing of circular discs between parallel plates, assuming that the collisions between discs, and between a disc and the wall, were instantaneous. In the latter case, wall roughness was incorporated by imposing (after collision) either (i) a zero relative velocity between the surface of the disc and the wall, or (ii) a zero relative velocity between the center of the disc and the wall. In both cases $\underline{\sigma}$ was asymmetric near the wall, and there were non-zero couple stresses.

Jenkins *et al.* [17] constructed a micro-mechanical model for an assembly of identical spheres. They found that asymmetric stresses resulted when the distribution of contact normals was anisotropic; however, they secured the symmetry of the stress tensor by suitably enforcing the rotation of particles.

Dry friction, the dominant mode of momentum transfer in high-density flows, introduces non-central forces in an inherently complex fashion. Hence, we expect that a micro-mechanical model for dry friction would result in a continuum with

asymmetric stresses; such materials can be modelled as Cosserat continua. A satisfactory micro-mechanical model is not yet available, and it is hoped that this issue will be addressed by future investigators.

2.1. Equations of motion. It is instructive to write the equations for the case of steady plane flow, and later simplify them for the case of fully developed flow. For flow parallel to the xy plane (figure 1), the velocity field has the following form:

$$v_x = v_x(x, y); v_y = v_y(x, y); v_z = 0; \omega_x = \omega_y = 0; \omega_z = \omega_z(x, y), \quad (1)$$

where v_x and ω_x are the x components of the linear and angular velocity, respectively. A positive value of ω_z is associated with an anti-clockwise rotation about the z -axis.

The balances for mass and linear momentum are

$$\frac{\partial}{\partial x}(\nu v_x) + \frac{\partial}{\partial y}(\nu v_y) = 0, \quad (2)$$

$$\frac{\partial \sigma_{xx}}{\partial x} + \frac{\partial \sigma_{yx}}{\partial y} + \rho_p \nu \left(v_x \frac{\partial}{\partial x} + v_y \frac{\partial}{\partial y} \right) v_x = 0, \quad (3)$$

$$\frac{\partial \sigma_{xy}}{\partial x} + \frac{\partial \sigma_{yy}}{\partial y} + \rho_p \nu \left(v_x \frac{\partial}{\partial x} + v_y \frac{\partial}{\partial y} \right) v_y = -\rho_p \nu g, \quad (4)$$

where ν is the solids fraction or the volume fraction of solids, σ_{ij} 's are the components of the Cauchy stress tensor, defined in the compressive sense, ρ_p is the intrinsic density of the particles, assumed constant, and g is the acceleration due to gravity.

Following Jaunzemis [13,p. 233], the z component of the angular momentum balance is

$$\frac{\partial M_{xz}}{\partial x} + \frac{\partial M_{yz}}{\partial y} - \rho_p \nu \zeta_z + \sigma_{xy} - \sigma_{yx} + \rho_p \nu \left(v_x \frac{\partial}{\partial x} + v_y \frac{\partial}{\partial y} \right) \eta_z = 0, \quad (5)$$

where M_{iz} 's are the couple stresses, η_z is the z component of the intrinsic angular momentum (per unit volume), and ζ_z is the z component of the body couple acting on the material.

To close the above set of equations, constitutive relations for the σ_{ij} and M_{iz} are required.

2.2. Constitutive equations. Mühlhaus and Vardoulakis [9] and Tejchman and Wu [6] have developed Cosserat plasticity models for studying the development of shear bands in granular flow. In their models, the yield condition and the flow rule were modified to account for the influence of the couple stress and to provide a relation for the angular velocity. We have adapted their model to the present problem. The constitutive equations comprise of a yield condition and a flow rule, which are elaborated below.

2.2.1. Yield condition. Following Besdo [18,cited in 19], de Borst [20], and Tejchman and Wu [6], we use a yield condition of the form

$$F \equiv \tau - Y = 0, \quad (6)$$

where

$$\tau \equiv \left(a_1 \sigma'_{ij} \sigma'_{ij} + a_2 \sigma'_{ij} \sigma'_{ji} + \frac{1}{(Ld_p)^2} M_{ij} M_{ij} \right)^{1/2}, \quad (7)$$

$\sigma'_{ij} = \sigma_{ij} - (1/3)\sigma_{kk}\delta_{ij}$ is the deviatoric stress, δ_{ij} is the Kronecker delta, a_1 , a_2 , and L are material constants, and d_p is the particle diameter. Here Ld_p is a characteristic material length scale; the value of L will be chosen later. de Borst [20] assumes that the yield limit Y depends on the mean stress $\sigma \equiv \sigma_{kk}/3$, and a hardening parameter h . Here we identify h with the solids fraction ν .

Schofield and Wroth [21,p. 112] and Jackson [1] discuss the use of a yield condition of the form $F(\underline{\sigma}, \nu) = 0$ in the classical frictional models. The yield condition (6) with $Y = Y(\sigma, \nu)$ represents an attempt to include couple stresses within this framework. Only two of the three parameters a_1 , a_2 and L in (7) are independent, because the third parameter may be absorbed in the definition of $Y(\sigma, \nu)$ (see (6)). Following Mühlhaus and Vardoulakis [9] we set $a_1 + a_2 = 1/2$, without loss of generality.

Tejchman and Wu [6] use $A \equiv a_2/a_1 = 1/3$ and $L = 1$. Here we retain their choice of A and treat L as an adjustable parameter, whose value is chosen as described later. de Borst [20] found that changes in the values of A and L affected the post-peak behaviour of a sample which was sheared between parallel plates. Unfortunately, neither experiments nor satisfactory micro-mechanical models are available to guide the choice of A .

Following Prakash and Rao [22], we assume the following form for the yield limit Y

$$Y = \sigma_c(\nu) \sin \phi \left(n\alpha - (n-1)\alpha^{n/(n-1)} \right); \quad \alpha \equiv \frac{\sigma}{\sigma_c(\nu)}. \quad (8)$$

Here $\sigma_c(\nu)$ is the mean stress at a critical state, ϕ is a material constant called the angle of internal friction, and n is a material constant. The significance of a critical state will be explained shortly. The dependence of σ_c on the solids fraction ν is taken to be [23]

$$\sigma_c(\nu) = \begin{cases} 0 & \nu < \nu_{\min}, \\ \Lambda \frac{(\nu - \nu_{\min})^p}{(\nu_{\max} - \nu)^q} & \nu_{\min} \leq \nu \leq \nu_{\max}. \end{cases} \quad (9)$$

Here Λ , ν_{\min} , ν_{\max} , p and q are material constants. Note that $\sigma_c(\nu)$ has been chosen to be zero below ν_{\min} , the solids fraction at loose random packing, and to diverge as ν approaches ν_{\max} , the solids fraction at dense random packing.

2.2.2. Flow rule. Tejchman and Wu [6] have used incremental elasto-plastic constitutive equations, which they attribute to Mühlhaus [11]. Elastic effects are ignored in the present work to simplify the analysis. Because we are interested in sustained flow, the plastic strain increments used by Tejchman and Wu [6] are replaced by suitable velocity gradients [11]. In Cartesian tensor notation, the flow rule is given by

$$E_{ij} \equiv \frac{\partial v_i}{\partial x_j} + \varepsilon_{ijk}\omega_k = \dot{\lambda} \frac{\partial G}{\partial \sigma_{ji}}; \quad H_{ij} \equiv \frac{\partial \omega_i}{\partial x_j} = \dot{\lambda} \frac{\partial G}{\partial M_{ji}}, \quad (10)$$

where $G(\underline{\sigma}, \underline{M}, \nu)$ is the plastic potential, ε_{ijk} is the alternating tensor, and $\dot{\lambda}$ is a scalar factor. We note here that E_{ij} is the sum of the rate of deformation tensor D_{ij} and an objective antisymmetric tensor representing the difference between the spin tensor and the particle spin $\varepsilon_{ijk}\omega_k$. E_{ij} and H_{ij} are conjugate to the stress σ_{ji} and the couple stress M_{ji} , respectively, in the sense that the rate of working per unit volume by the contact forces and couples is given by $-(\sigma_{ji}E_{ij} + M_{ji}H_{ij})$ [11]. In

a classical continuum, \underline{M} vanishes and $\underline{\sigma}$ is symmetric; hence the above expression reduces to $-\sigma_{ji}D_{ij}$, where $D_{ij} = (1/2)(\partial v_i/\partial x_j + \partial v_j/\partial x_i)$ denotes a component of the rate of deformation tensor.

Lacking detailed information on the plastic potential G , we adopt the most commonly used closure, namely the associated flow rule [21,p. 43]:

$$G \equiv F = \tau - Y. \quad (11)$$

This form of the flow rule accounts for density changes accompanying deformation.

3. APPLICATION TO CHANNEL FLOW

For the case of steady, fully developed, plane flow, the velocity field is given by

$$v_y = v_y(x); \quad \omega \equiv \omega_z(x), \quad (12)$$

and the other velocity components vanish. Hence the mass balance (2) is identically satisfied and the balances of linear and angular momentum (3)–(5) reduce to

$$\frac{d\sigma_{xx}}{dx} = 0; \quad \frac{d\sigma_{xy}}{dx} = -\rho_p \nu g, \quad (13)$$

$$\frac{dm}{dx} + \sigma_{xy} - \sigma_{yx} = 0, \quad (14)$$

where $m \equiv M_{xz}$. It is assumed that the yield condition is satisfied at every point in the channel, so that the factor $\dot{\lambda}$ in (10) is always non-zero. In writing (14), it is assumed that there are no body couples.

3.1. The stress field. For fully developed flow, it will now be shown that all the normal stresses are equal. Equation (10) implies that

$$E_{xx} = \frac{\partial v_x}{\partial x} = 0 = \frac{\dot{\lambda}}{6\tau}(2\sigma'_{xx} - \sigma'_{yy} - \sigma'_{zz}) - \frac{\dot{\lambda}}{3} \frac{\partial Y}{\partial \sigma}. \quad (15)$$

Writing the corresponding equations for E_{yy} and E_{zz} and summing, we get

$$\frac{\partial Y}{\partial \sigma} = 0, \quad (16)$$

or using (8)

$$\sigma = \sigma_c(\nu); \quad Y = \sigma_c \sin \phi. \quad (17)$$

Thus the material is at a critical state or a state of isochoric deformation, because $E_{ii} = \nabla \cdot \underline{v} = 0$. Comparison of (8) and (17) shows that the value of n is not relevant. It also follows from (15), (17) and (13) that

$$\sigma_{xx} = \sigma_{yy} = \sigma_{zz} = \sigma_c(\nu) = \text{constant}. \quad (18)$$

Hence the solids fraction does not vary across the width of the channel.

Using (17) and (18), the yield condition (6) reduces to

$$\left(a_1(\sigma_{xy}^2 + \sigma_{yx}^2) + 2a_2\sigma_{xy}\sigma_{yx} + \frac{m^2}{(Ld_p)^2} \right)^{1/2} - \sigma_c(\nu) \sin \phi = 0. \quad (19)$$

3.2. Velocity field. The non-trivial equations of the flow rule (10) are

$$E_{xy} = \omega = \frac{\dot{\lambda}}{\tau} (a_1 \sigma_{yx} + a_2 \sigma_{xy}), \quad (20)$$

$$E_{yx} = \frac{dv_y}{dx} - \omega = \frac{\dot{\lambda}}{\tau} (a_1 \sigma_{xy} + a_2 \sigma_{yx}), \quad (21)$$

$$H_{zx} = \frac{d\omega}{dx} = \frac{\dot{\lambda}}{\tau} \frac{m}{(Ld_p)^2}. \quad (22)$$

On eliminating $\dot{\lambda}$ we get

$$\frac{dv_y}{dx} = \frac{(A+1)(\sigma_{xy} + \sigma_{yx})\omega}{\sigma_{yx} + A\sigma_{xy}}, \quad (23)$$

$$\frac{d\omega}{dx} = \frac{2(A+1)m\omega}{(Ld_p)^2(\sigma_{yx} + A\sigma_{xy})}. \quad (24)$$

3.3. Boundary conditions. Considering symmetric solutions, we have

$$\sigma_{xy}(0) = 0; \quad \omega(0) = 0. \quad (25)$$

The angular velocity ω must vanish at the centerline of the channel, because a non-zero value implies a preferred direction of rotation.

Equations (20) and (25) imply

$$\sigma_{yx}(0) = 0, \quad (26)$$

provided $m(0)$ is bounded, i.e., $\nu < \nu_{\max}$ (see (7), (9), and (19)). Because σ_{xy} and σ_{yx} both vanish at the centerline, the yield condition (19) implies that the couple stress at the centerline is

$$m(x=0) = \pm Ld_p \sigma_c \sin \phi. \quad (27)$$

While both roots in (27) are mathematical solutions, only the negative root yields a physically reasonable solution. The justification for choosing this root, and the reason for discarding the other are discussed in Appendix A.

At the right hand wall $x = W$ we use the usual friction boundary condition ([24]; [25, p. 40])

$$-\frac{\sigma_{xy}}{\sigma_{xx}} = \tan \delta \quad \text{at } x = W, \quad (28)$$

where δ is a constant called the angle of wall friction. Using (13) and (18), (28) reduces to

$$\frac{\rho_p \nu g W}{\sigma_c(\nu)} = \tan \delta \quad \text{at } x = W, \quad (29)$$

which determines the value of ν for specified values of W and δ .

Following Tejchman and Gudehus [5], we assume that

$$v_y = -Kd_p \omega \quad \text{at } x = W, \quad (30)$$

where K is a dimensionless constant which reflects the roughness of the wall. To get a feel for this condition, consider a single spherical particle sliding or rolling down a vertical wall. Let v'_y and ω' represent the linear velocity of the center of the particle and its angular velocity about an axis through its center, respectively. If the particle slides without rolling, $\omega' = 0$, but v'_y is arbitrary. Conversely, if it rolls without slipping $|v'_y| = (d_p/2) |\omega'|$. For the boundary condition (30), these limits

correspond to $K \rightarrow \infty$ and $K \rightarrow 1/2$, respectively. Reverting to the continuum, we expect that K will decrease as the wall roughness increases.

One more boundary condition is needed to permit determination of all the integration constants. Here we set

$$\omega(x = W) = \omega_w, \quad (31)$$

where ω_w is a constant whose value is determined by adjusting either the mass flow rate or the centerline velocity to match the measured value. In experiments, the mass flow rate may be varied within limits by varying the width $2W_s$ of the exit slot at the bottom of the channel. Because we are considering fully developed flow, W_s does not occur explicitly in the governing equations, but its influence is incorporated by changing ω_w .

4. SOLUTION PROCEDURE

Introducing the dimensionless variables

$$\begin{aligned} \xi &= \frac{x}{W}; & \epsilon &= \frac{d_p}{W}; & u &= -\frac{v_y}{(gW)^{1/2}}; \\ \bar{\omega} &= \omega \left(\frac{W}{g} \right)^{1/2}; & \bar{\sigma}_{ij} &= \frac{\sigma_{ij}}{\rho_p g W}; & \bar{m} &= \frac{m}{\rho_p g W d_p}, \end{aligned}$$

the balance equations (13) and (14) may be rewritten as

$$\frac{d\bar{\sigma}_{xx}}{d\xi} = 0, \quad (32)$$

$$\frac{d\bar{\sigma}_{xy}}{d\xi} = -\nu, \quad (33)$$

$$\epsilon \frac{d\bar{m}}{d\xi} + \bar{\sigma}_{xy} - \bar{\sigma}_{yx} = 0, \quad (34)$$

where ν is the constant solids fraction across the channel, and

$$\epsilon \equiv \frac{d_p}{W}. \quad (35)$$

The dimensionless form of the yield condition (19) is

$$a_1(\bar{\sigma}_{xy}^2 + \bar{\sigma}_{yx}^2) + 2a_2\bar{\sigma}_{xy}\bar{\sigma}_{yx} + \frac{\bar{m}^2}{L^2} = (\bar{\sigma}_c \sin \phi)^2. \quad (36)$$

Here $\bar{\sigma}_c(\nu) = \sigma_c/(\rho_p g W)$. The flow rule (23) and (24) is given by

$$\frac{du}{d\xi} = -\frac{(1+A)(\bar{\sigma}_{xy} + \bar{\sigma}_{yx})\bar{\omega}}{\bar{\sigma}_{yx} + A\bar{\sigma}_{xy}}, \quad (37)$$

$$\frac{d\bar{\omega}}{d\xi} = \frac{2(1+A)\bar{m}\bar{\omega}}{\epsilon L^2(\bar{\sigma}_{yx} + A\bar{\sigma}_{xy})}. \quad (38)$$

The boundary conditions are:
at the centerline ($\xi = 0$)

$$\bar{\sigma}_{xy} = 0; \quad \bar{\omega} = 0. \quad (39)$$

at the wall ($\xi = 1$)

$$\frac{\nu}{\bar{\sigma}_c(\nu)} = \tan \delta; \quad u = \epsilon K \bar{\omega}. \quad (40)$$

Equations (26) and (27) may be written as

$$\bar{\sigma}_{yx} = 0, \quad \bar{m} = -NL\nu \quad \text{at} \quad \xi = 0, \quad (41)$$

where $N \equiv \sin \phi / \tan \delta$, and (40) has been used to simplify the second of equations (41).

4.1. Method of solution. For the special case $A = -1$, an analytical solution may be obtained as discussed in Appendix A. This shows that $\bar{m} = \text{constant}$, $\bar{\sigma}_{yx} = \bar{\sigma}_{xy}$, and $\bar{\omega}$ and $u - u(0)$ display a power law dependence on ξ . (The case $A < -1$ is discussed in Appendix A.)

We now discuss the case $A > -1$. Inspection of (32)–(41) shows that the stress field is uncoupled from the velocity field. Hence we first integrate the equations (32), (33) and (39). Equations (32) and (33) may be solved along with the first of boundary conditions (39) to get

$$\bar{\sigma}_{xx} = \text{constant}; \quad \bar{\sigma}_{xy} = -\nu\xi. \quad (42)$$

The yield condition (36) may be solved for $\bar{\sigma}_{yx}$ to get

$$\bar{\sigma}_{yx} = A\nu\xi \mp \left((A^2 - 1)(\nu\xi)^2 + 2(A + 1) \left(N^2\nu^2 - \frac{\bar{m}^2}{L^2} \right) \right)^{1/2}. \quad (43)$$

In our calculations, only the root with the negative sign before the square root term in (43) was chosen. The justification for doing so is described in Appendix A. After substituting this expression for $\bar{\sigma}_{yx}$ in (34), we solve the equation along with the boundary conditions (41) as an initial value problem by marching from $\xi = 0$ to $\xi = 1$.

Equation (34) is solved numerically using the LSODA routine [26] from ODEPACK in NETLIB. It should be noted that the above package estimates \bar{m} at a small distance ξ_1 from $\xi = 0$ as

$$\bar{m}(\xi_1) \approx -NL\nu + \frac{d\bar{m}}{d\xi}(0) \xi_1 = -NL\nu,$$

because (41) and (34) imply that $\frac{d\bar{m}}{d\xi}(0) = 0$. This causes the term under the square root in (43) to be negative. To avoid this problem (34) is integrated numerically from $\xi = \xi_1$ to $\xi = 1$, with the initial condition given by

$$\bar{m}(\xi_1) = -NL\nu + \frac{1}{2} \frac{d^2\bar{m}}{d\xi^2}(0) \xi_1^2,$$

with $\xi_1 = 10^{-5}$. The use of a smaller value of ξ_1 does not significantly affect the results.

Here $\frac{d^2\bar{m}}{d\xi^2}(0)$ is calculated by differentiating (34) with respect to ξ , and using (42) and (43). The resulting indeterminate expression is evaluated using the L'Hospital's rule to get

$$\epsilon \frac{d^2\bar{m}}{d\xi^2}(0) = (A + 1)\nu \mp \nu \left(A^2 - 1 + 2(A + 1) \frac{N}{L\nu} \frac{d^2\bar{m}}{d\xi^2}(0) \right)^{1/2}. \quad (44)$$

This can be rearranged to get a quadratic equation for $\frac{d^2\bar{m}}{d\xi^2}(0)$, and we choose the root that satisfies

$$\epsilon \frac{d^2\bar{m}}{d\xi^2}(0) \leq (A + 1)\nu,$$

as the other root is inconsistent with (49).

Once the stresses are obtained, the velocities are calculated by integrating the flow rule (37) and (38) from $\xi = 1$ to $\xi = 0$ using the initial conditions (40). The integration is started from $\xi = 1$ because

$$B(\xi) \equiv \frac{2(1 + A)\bar{m}}{\epsilon L^2(\bar{\sigma}_{yx} + A\bar{\sigma}_{yx})} \quad (45)$$

becomes unbounded as $\xi \rightarrow 0$, and hence the right hand side of (38) is indeterminate at $\xi = 0$.

Equation (38) is therefore integrated from $\xi = 1$ to get

$$\bar{\omega}(\xi) = \bar{\omega}_w \exp\left(-\int_{\xi}^1 B(\xi') d\xi'\right), \quad (46)$$

where $\bar{\omega}_w = \omega_w(W/g)^{1/2}$ is the dimensionless angular velocity at the wall. It is shown in Appendix B that $\int_{\xi}^1 B(\xi') d\xi'$ becomes unbounded as $\xi \rightarrow 0$. Hence $\bar{\omega}$ satisfies the boundary condition $\bar{\omega}(0) = 0$ for all finite values of $\bar{\omega}_w$.

It is also of interest to determine the behaviour of the solutions in the limit $\epsilon \equiv d_p/W \rightarrow 0$. The issue here is the scaling of the shear layer thickness as a function of the channel half-width, W . For small ϵ , an asymptotic solution is constructed using a perturbation technique described in Appendix C. The predictions of this solution are discussed in the next section along with the numerical results.

4.1.1. *Parameter values.* The intrinsic density of the particles (ρ_p) was taken from the studies of Nedderman and Laohakul [3], Natarajan *et al.* [27] and Tüzün and Nedderman [28]. Glass beads were used in all the experiments. For want of data, the angle of internal friction ϕ was taken to be equal to the reported angle of repose.

The parameters ν_{\min} and ν_{\max} were chosen to be 0.5 and 0.65, respectively. The parameters in (9) were estimated as follows. Jyotsna and Rao [29] used the data of Fickie *et al.* [30] to obtain an expression for the variation of the mean stress at a critical state (σ_c) as a function of the solids fraction ν . This expression was used to generate the values of $\bar{\sigma}_c$ for ν in the range 0.54–0.58, and the latter were used to estimate $\Lambda/(\rho_p g W)$, p and q by the method of nonlinear least squares, using the Marquardt-Levenberg algorithm [31, p. 678]. The parameter values were found to be $\Lambda/(\rho_p g W) = 817$, $p = 2.5$, and $q = 2.2$.

In the experiments of Nedderman and Laohakul [3] and Natarajan *et al.* [27], a layer of particles was stuck to the walls of the channel. This will be referred to as a fully rough wall. When we compare model predictions with their data, the angle of wall friction is chosen as $\delta = \tan^{-1}(\sin \phi)$ [32]. For comparing the predictions with stress measurements of Tüzün and Nedderman [28], the measured angle of wall friction, $\delta = 10^\circ$, was used.

The value of the parameter L , which occurs in the yield condition (36) was estimated to be 10 by matching predicted velocity profiles with the data of Nedderman and Laohakul [3] (see figure 2). This value was used in comparisons with all other data. The parameter K was set to 0.5.

5. RESULTS

In this section we compare the predictions of the theory with the data of Nedderman and Laohakul [3], Natarajan *et al.* [27], and Tüzün and Nedderman [28].

5.1. Velocity profiles. With $L = 10$, there is a good match between predicted and measured linear velocity profiles of Nedderman and Laohakul [3] (figure 2). (Predictions of the theory with $L = 2$ and $L = 20$ are also shown in figure 2 for comparison.) The solids fraction of 0.60 predicted by the model is in close agreement with the measured average value of 0.61.

While there is no sharply defined plug layer in the model (and in the experiments), there is a region of low shear rate near the center of the channel. In order to compare predictions with the data of Nedderman and Laohakul [3], the apparent thickness of the “plug” layer, ξ_p is calculated from

$$\frac{u(\xi_p)}{u(\xi = 0)} = 0.95. \quad (47)$$

Hence the shear layer thickness, scaled by the particle diameter is $\Delta \equiv (1 - \xi_p)(W/d_p)$. The model predicts a central plug layer and a shear layer adjacent to the wall whose thickness is about 10.5 particle diameters.

With $L = 10$, the predicted velocity profile also agrees well with the data of Natarajan *et al.* [27] as shown in figure 3. This is an encouraging result because the ratio of the channel width to the particle diameter differs by a factor of 3.5 for the two sets of data. For the profile shown in figure 3, the solids fraction of 0.59 lies in the range 0.55–0.67 estimated from the experiments.

The open circles in figures 2 and 3 show the asymptotic velocity profiles for small ϵ — the deviation from the numerical solution is greater in figure 3 because ϵ is larger than that in figure 2. For $\epsilon = 1/600$, the asymptotic solution is indistinguishable from the numerical solution, as shown in figure 4.

The angular velocity ($\bar{\omega}$) profile, shown in figure 5, differs slightly from that of half the dimensionless vorticity $(1/2) du/d\xi$. As expected, the difference is more pronounced in the shear layer. (In a classical continuum, $(1/2) du/d\xi$ represents the local angular velocity of an infinitesimal spherical material volume.) The asymptotic solution deviates significantly from the numerical solution for $\epsilon = 1/30$ (figure 5), but the two solutions agree well for $\epsilon = 1/600$ (figure 6).

5.2. Influence of channel width on the thickness of the shear layer. For a fixed value of the particle diameter d_p , the thickness of the shear layer Δ increases with the half-width of the channel W (solid line in figure 7). This is roughly in accord with the data of Nedderman and Laohakul [3], which are represented by solid symbols in figure 7. For each value of the W/d_p , there are three data points; these correspond to the estimates of Δ obtained by fitting three different functional forms to the measured velocity profile.

For small values of $\epsilon = d_p/W$, the perturbation solution (Appendix C) shows that

$$\Delta \sim \left(\frac{L^2}{2}\right)^{1/3} \epsilon^{-1/3}.$$

Thus the dimensional thickness of the shear layer is proportional to $(d_p/W)^{-1/3}$ when $d_p/W \ll 1$, and hence does not attain a constant value in this limit. It would

be interesting to conduct experiments with much larger values of W/d_p than in the range shown in figure 7. This would permit a more stringent test of the model predictions.

5.3. Influence of the parameter L on the thickness of the shear layer.

As mentioned earlier, the length scale Ld_p was chosen to fit the model predictions to the data of Nedderman and Laohakul [3]. It is important to know how the predictions vary with changes in this parameter. Figure 8 shows that the thickness of the shear layer is a weak function of L . In the limit of small ϵ , the shear layer thickness varies as $L^{2/3}$ (Appendix C).

5.4. Influence of the wall-roughness factor K on thickness of the shear layer.

The variation of the shear layer thickness with the roughness parameter K is shown in figure 9. As mentioned earlier, $K \rightarrow \infty$ corresponds to a very smooth wall; it decreases as the wall roughness increases. Figure 9 shows that there is little variation with K of the shear layer thickness for small K , but significant variation in the range ≈ 1 –200. For K greater than 200, the velocity at the wall is greater than 95% of the centerline velocity. Hence, by our definition (47), the thickness of the shear layer is zero. As shown in Appendix C, the shear layer thickness is independent of K in the limit of small ϵ .

5.5. Stresses.

5.5.1. *Stress profiles.* Figure 10 shows the profiles of the shear stresses $\bar{\sigma}_{xy}$ and $\bar{\sigma}_{yx}$ for $\epsilon = 1/30$ and $1/600$. It is clear that the difference between $\bar{\sigma}_{xy}$ and $\bar{\sigma}_{yx}$ increases with ξ . Because $\bar{\sigma}_{yx} > \bar{\sigma}_{xy}$, the couple stress \bar{m} also increases with ξ (figure 11), in accord with (34).

The open symbols in figures 10 and 11 represent the asymptotic solution for small ϵ . When $\epsilon = 1/600$, it is clear that the asymptotic solution is indistinguishable from the exact solution, and the difference $\bar{\sigma}_{xy} - \bar{\sigma}_{yx}$ is also very small.

5.5.2. *Wall stresses.* We now compare the predicted wall stresses with the data of Tüzün and Nedderman [28] (Table 1). The normal and shear stresses are over-predicted, but are of the same order of magnitude as the measured values. As noted by Mohan *et al.* [7], the dimensions of the channel used in the experiments are such that the front and the back faces may support a significant part of the weight of the material. Hence the shear stress measured at the side wall is expected to be less than the prediction, which assumes a channel of infinite depth. It is interesting to note that the estimate of Tüzün and Nedderman [28] for the average solids fraction is 0.63 and the model predicts a value of 0.625.

6. COMPARISON WITH OTHER MODELS

6.1. **The classical frictional model.** The classical frictional model predicts a flat velocity profile. This is consistent with the profile predicted by the Cosserat model in the limit $d_p \rightarrow 0$ for a fixed value of W . Further, the Cosserat continuum reduces to the classical continuum in this limit, because $m \rightarrow 0$ and $\sigma_{xy} \rightarrow \sigma_{yx}$.

	H	Normal stress		Shear stress	
		Static	Flowing	Static	Flowing
Experiments	0.91	2.7–3.6	4.0–5.1	0.30–0.39	0.29–0.35
	1.07	2.7–2.9	3.8–4.6	0.30	0.41–0.58
	1.22	2.7–3.6	4.6–5.7	0.52–0.65	0.58–0.76
Cosserat model	—	—	7.97	—	1.12
Kinetic model	—	—	2.51	—	1.15

Table 1. Comparison of predicted wall stresses with the data of Tüzün and Nedderman [28] for glass beads. Here H is the depth measured from the top of the channel. Units: H – m, stress– kN/m². Parameter values: $W = 0.155$ m, $d_p = 2.29$ mm, $\rho_p = 1180$ kg/m³, $\phi = 30^\circ$, $\delta = 8^\circ$.

6.2. The kinetic and frictional-kinetic models. The broken curves in figure 7 show the results obtained by using the (high density) kinetic model and the frictional-kinetic model. For these models we have used the equations given in Mohan *et al.* [7], except that the mean stress at critical state (σ_c in their paper) is evaluated using (9).

The kinetic model is based on constitutive equations derived by using the kinetic theory of dense gases [see, for example, 10]. Two of the underlying assumptions of this theory, namely instantaneous binary collisions between particles and molecular chaos with respect to particle velocities, are expected to break down at high solids fractions. Therefore it is surprising, and perhaps fortuitous, that the predicted thickness of the shear layer is in fair agreement with the data (figure 7) even though the solids fraction is in the range of 0.64–0.65.

Based on the results shown in figure 7, it is difficult to discriminate between the Cosserat and the kinetic models. It should be noted that both these models contain a material length scale in their constitutive equations. As noted by Tejchman and Wu [12], this may be a pre-requisite for a satisfactory description of shear layers.

The frictional-kinetic model is constructed by assuming that the stress tensor is the sum of the kinetic stress tensor and the frictional stress tensor. This model grossly underestimates the thickness of the shear layer (see the dotted curve in figure 7), probably because (i) frictional effects dominate kinetic effects in the shear layer, and (ii) the frictional constitutive equations do not contain a material length scale.

6.3. The model of Tejchman and Gudehus [5]. The work of Tejchman and Gudehus [5] appears to be the only other study which uses a Cosserat model for channel flow. They use an elasto-plastic model to examine the batch discharge of material from a cylindrical bin. The constitutive equations involve the Jaumann stress rate and the ‘velocity strain’ tensor. Since they do not present results for steady fully developed flow, a direct comparison of our predictions with theirs is not possible. We are currently attempting to use their model for the problem at hand, but some issues require consideration before results can be obtained. For example, Dienes [33] have reported that the Jaumann stress rate furnishes an unrealistic oscillatory response in simple shear for a hypoelastic model.

7. DISCUSSION

Unlike the classical frictional model [7], the present Cosserat model predicts velocity profiles which agree well with the data of Nedderman and Laohakul [3] and Natarajan *et al.* [27]. Further, the variation of the thickness of the shear layer with the width of the channel is also captured reasonably well by the model. The predicted wall stresses are of the same order of magnitude as the measured values, but there is considerable scope for improvement. In this context, it may be desirable to account for the finite spacing between the front and back walls.

Our solution of the model for the limiting case of an infinitely wide channel ($\epsilon \rightarrow 0$) with fully rough walls indicates that the shear layer thickness, scaled by the particle diameter, grows as $\epsilon^{-1/3}$, where ϵ is the ratio of the particle diameter to the channel width. It would be interesting to compare this result with experiments conducted for a wide range of ϵ .

In the present work, and in most applications of the frictional Cosserat models, *ad hoc* values are prescribed for the parameters a_1 , a_2 , and L in the yield condition (7). Either suitably designed experiments, or a micro-mechanical treatment, would be valuable in providing estimates for these parameters. Similarly, it would be desirable to have a micro-mechanical basis for the kinematic boundary condition (30). An unsatisfactory feature of our model is that the solids fraction is constant across the channel. This is in variance with qualitative observations of Natarajan *et al.* [27] that the density in the shear layer is lower than that in the plug region. Perhaps the inclusion of elastic or kinetic effects in the model would correct this feature. In any case, accurate density measurements in channel flow are lacking, and more investigations in this direction are needed.

APPENDIX A. CHOICE OF SIGNS IN (27) AND (43)

In sections 3 and 4 it was mentioned that only the negative root of (27) was chosen in our calculations, and that only one of two possible choices was made in the sign for the square root in (43). In this appendix we discuss the justification for doing so.

Rewriting the angular momentum balance (34) by substituting for $\bar{\sigma}_{yx}$ from (43), we get

$$\epsilon \frac{d\bar{m}}{d\xi} = (A + 1)\nu\xi + D^{1/2} \equiv E_+, \quad (48)$$

$$\epsilon \frac{d\bar{m}}{d\xi} = (A + 1)\nu\xi - D^{1/2} \equiv E_-, \quad (49)$$

where

$$D = (A^2 - 1)\nu^2\xi^2 + 2(A + 1) \left(N^2\nu^2 - \frac{\bar{m}^2}{L^2} \right), \quad (50)$$

and $N \equiv \sin \phi / \tan \delta$. Equations (48) and (49) have to be integrated subject to the initial condition

$$\bar{m}(0) = \pm NL\nu, \quad (51)$$

The qualitative behaviour of the solutions to (48), (49), and (51) may be understood by examining the phase plane of (48) and (49), such as that shown in figure 12.

For $A < 1 - 2N^2$, $D < 0$ at $\xi = 1$. Hence (48) and (49) cannot be integrated till the wall ($\xi = 1$).

For $A > -1$ a real valued solution for (48) cannot be constructed using the initial condition $\bar{m}(0) = NL\nu$, because $E_+ \geq 0$ in the region bounded by the curves $D = 0$, and $D < 0$ outside this region (see figure 12). Suppose that the other initial condition $\bar{m}(0) = -NL\nu$ is used. For sufficiently small values of ϵ , the trajectory touches the upper curve $D = 0$ before reaching the channel wall (see, for example, the dot-dashed line in figure 12). Hence (48) is discarded. Using a similar approach, it follows that a suitable solution can be constructed for (49) only when the initial condition $\bar{m}(0) = -NL\nu$ is used. A typical trajectory is shown by the dotted line in figure 12. This choice of roots works only for small values of ϵ ; for the parameters used in figure 12, solutions could not be constructed for $\epsilon = 0.33$.

For $1 - 2N^2 < A < -1$, and small enough ϵ , it is possible to construct a solution for (48), subject to the initial condition $\bar{m}(0) = NL\nu$.

For $A = -1$, it follows from (48) and (49), and (34) that $\bar{m} = \text{constant} = -NL\nu$, $\bar{\sigma}_{xy} = \bar{\sigma}_{yx} = -\nu\xi$, and the velocity profiles are given by

$$\begin{aligned}\bar{\omega} &= \bar{\omega}_w \xi^{2N/(\epsilon L)}, \\ u &= u(0) - \frac{2\bar{\omega}_w \xi^{2N/(\epsilon L)+1}}{2N/(\epsilon L) + 1}.\end{aligned}$$

The other root $\bar{m}(0) = NL\nu$ is discarded because $\bar{\omega}(0)/\bar{\omega}_w \rightarrow \infty$ as $\xi \rightarrow 0$.

APPENDIX B. INTEGRATION OF (38)

In § 4.1 it was noted that $\bar{\omega}(0) = 0$ because $\lim_{\xi \rightarrow 0} \int_{\xi}^1 B(\xi') d\xi' = \infty$, where $B(\xi)$ is defined by (45). This is shown below.

Near $\xi = 0$, the leading order behaviour of the stresses can be represented as

$$\begin{aligned}\bar{\sigma}_{xy} &= -\nu\xi, \\ \bar{\sigma}_{yx} &= \bar{\sigma}'_{yx,0} \xi + O(\xi^2), \\ \bar{m} &= \bar{m}(0) + O(\xi^2),\end{aligned}$$

where

$$\bar{\sigma}'_{yx,0} \equiv \left. \frac{d\bar{\sigma}_{yx}}{d\xi} \right|_{\xi=0}.$$

The integral can now be written as

$$\lim_{\xi \rightarrow 0} \int_{\xi}^1 B(\xi') d\xi' = \lim_{\xi \rightarrow 0} \int_{\xi}^{\alpha} \frac{2(A+1)\bar{m}(0)}{(\bar{\sigma}'_{yx,0} - A\nu)\xi'} d\xi' + \int_{\alpha}^1 B(\xi') d\xi', \quad (52)$$

$$= \lim_{\xi \rightarrow 0} \frac{2(A+1)\bar{m}(0)}{(\bar{\sigma}'_{yx,0} - A\nu)} \ln \left(\frac{\alpha}{\xi} \right) + \int_{\alpha}^1 B(\xi') d\xi', \quad (53)$$

where α is a small positive number. When $A > -1$, and $\bar{m}(0)$ and $\bar{\sigma}_{yx}$ are evaluated as discussed in Appendix A, it follows from (34) and (44) that the factor multiplying the logarithm in (53) is positive, and hence the expression in (53) becomes unbounded.

APPENDIX C. ASYMPTOTIC SOLUTION FOR THE COSSERAT MODEL

Here we derive an asymptotic solution for the case of a fully rough wall (i.e., one for which $\tan \delta = \sin \phi$, or $N = 1$), in the limit $\epsilon \rightarrow 0$.

Using (40), (41), and (43), (34) may be rewritten as

$$\epsilon \frac{d\bar{m}}{d\xi} - (A+1)\nu\xi + \left((A^2-1)(\nu\xi)^2 + 2(A+1) \left(\nu^2 - \frac{\bar{m}^2}{L^2} \right) \right)^{1/2} = 0. \quad (54)$$

We now seek a solution for \bar{m} of the form

$$\bar{m} = m_0 + \epsilon m_1 + \epsilon^2 m_2 + \dots \quad (55)$$

Substituting this in (54), expanding the term under the square root for small ϵ , and collecting terms of $O(1)$ and $O(\epsilon)$ we get

$$m_0 = -L\nu(1-\xi^2)^{1/2}; \quad m_1 = -\frac{L^2\nu^2\xi^2}{2(1-\xi^2)}. \quad (56)$$

Equation (56) shows that the solution for \bar{m} is not uniformly valid as $|\epsilon m_1/m_0| \sim O(1)$ when $\xi \approx 1 - (1/2)\epsilon^{2/3}$.

To get an uniformly valid first approximation for \bar{m} , we proceed as suggested by Van Dyke [34,p. 104]. Introducing new variables

$$\xi' \equiv (1-\xi)\epsilon^{-2/3}; \quad m' \equiv \bar{m}\epsilon^{-1/3},$$

such that they are $O(1)$ in the inner region, we seek a solution of the form

$$m' = m'_0 + f(\epsilon)m'_1 + \dots \quad (57)$$

Substituting (57) in (54), expanding the term under the square root for small ϵ , and collecting terms of $O(1)$, we get

$$\frac{dm'_0}{d\xi'} = 2\nu\xi' - \frac{m'^2_0}{\nu L^2}. \quad (58)$$

Equation (58) is a Riccati equation [35,p. 20], which can be converted to a second-order linear differential equation by using the transformation

$$m'_0(\xi') = \frac{\nu L^2 dm''_0/d\xi'}{m''_0(\xi')} \quad (59)$$

to get

$$\frac{d^2 m''_0}{d\xi'^2} = \frac{2\xi'}{L^2} m''_0. \quad (60)$$

Using the transformation $\bar{\xi} \equiv (2/L^2)^{1/3} \xi'$, (60) reduces to the Airy equation

$$\frac{d^2 m''_0}{d\bar{\xi}^2} = \bar{\xi} m''_0, \quad (61)$$

and its general solution is given by [35,p. 100]

$$m''_0 = C_1 \text{Ai}(\bar{\xi}) + C_2 \text{Bi}(\bar{\xi}). \quad (62)$$

Here Ai and Bi are the linearly independent Airy functions, and C_1 and C_2 are integration constants. Hence

$$m'_0 = \left(\frac{2}{L^2} \right)^{1/3} \frac{\nu L^2}{C_1 \text{Ai}(\bar{\xi}) + C_2 \text{Bi}(\bar{\xi})} \frac{d}{d\bar{\xi}} (C_1 \text{Ai}(\bar{\xi}) + C_2 \text{Bi}(\bar{\xi})). \quad (63)$$

To determine C_1 and C_2 , we follow the procedure discussed in Van Dyke [34,p. 105]. The outer solution (56) is rewritten in terms of the inner variable and expanded for small ϵ to get the leading order inner expansion of the outer solution

$$-L\nu\epsilon^{1/3} (2\xi')^{1/2}.$$

Similarly, the inner solution should be rewritten in terms of the outer variables and expanded for small ϵ . This is exactly equivalent to expanding (63) in the limit $\bar{\xi} \rightarrow \infty$. The leading order outer expansion of the inner solution is

$$\begin{aligned} -L\nu\epsilon^{1/3} (2\xi')^{1/2} & \text{ if } C_2 = 0; \\ L\nu\epsilon^{1/3} (2\xi')^{1/2} & \text{ if } C_1 = 0, \end{aligned}$$

where the asymptotic expansions of the Airy function [35,p. 100] have been used. Thus the inner and outer expansions have the same functional behaviour in the ‘‘overlap’’ region provided $C_2 = 0$; hence

$$m_0'' = C_1 \text{Ai}(\bar{\xi}). \quad (64)$$

Following the procedure described in Van Dyke [34,p. 94], the leading order composite (additive) solution is given by

$$\bar{m} = -L\nu(1 - \xi^2)^{1/2} + \left(\frac{2\epsilon}{L^2}\right)^{1/3} \frac{1}{\text{Ai}(\bar{\xi})} \frac{d\text{Ai}}{d\bar{\xi}} + \nu L(2(1 - \xi))^{1/2}. \quad (65)$$

Similarly, the composite solution for the other variables is given by

$$\bar{\sigma}_{yx} = -2\nu + \nu\xi + \left(\frac{2\epsilon^2}{L^2}\right)^{1/3} \frac{1}{L^2\nu\text{Ai}(\bar{\xi})} \frac{d\text{Ai}}{d\bar{\xi}}, \quad (66)$$

$$\bar{\omega} = \bar{\omega}_w \left(\frac{\text{Ai}(\bar{\xi})}{\text{Ai}(0)}\right)^2, \quad (67)$$

$$u = 2\bar{\omega}_w \left(\frac{2\epsilon^2}{L^2}\right)^{1/3} I(\bar{\xi}), \quad (68)$$

where

$$I(\bar{\xi}) = \int_0^{\bar{\xi}} \left(\frac{\text{Ai}(z)}{\text{Ai}(0)}\right)^2 dz.$$

The parameter $\bar{\omega}_w = \bar{\omega}(\xi = 1) = \bar{\omega}(\bar{\xi} = 0)$ is determined as follows. Using (68) and the measured centerline velocity $u_e(\xi = 0)$, we get

$$\bar{\omega}_w = \frac{u_e(\xi = 0)}{2\left(\frac{2\epsilon^2}{L^2}\right)^{1/3} I(\bar{\xi}_0)}, \quad (69)$$

where $\bar{\xi}_0 = (2/L^2)^{1/3}\epsilon^{-2/3}$.

Using (47), (68) and (69), the thickness ξ_p of the plug is given by

$$\frac{u(\xi_p)}{u(\xi = 0)} = \frac{I(\bar{\xi}_p)}{I(\bar{\xi}_0)} = 0.95,$$

where $\bar{\xi}_p = (1 - \xi_p)(2/L^2)^{1/3}\epsilon^{-2/3}$.

In the limit $\epsilon \rightarrow 0$, $\bar{\xi}_0 \rightarrow \infty$ and $I(\bar{\xi}_0)$ tends to a constant. Hence, for small ϵ , $\bar{\xi}_p$ is approximately independent of ϵ , and $\lim_{\epsilon \rightarrow 0} \bar{\xi}_p = 1.275$. The dimensionless shear layer thickness is therefore given by

$$1 - \xi_p = \left(\frac{L^2}{2}\right)^{1/3} \epsilon^{2/3} \bar{\xi}_p,$$

and the shear layer thickness expressed in terms of particle diameter is

$$\Delta \equiv (1 - \xi_p) \frac{W}{d_p} = \left(\frac{L^2}{2}\right)^{1/3} \epsilon^{-1/3} \bar{\xi}_p.$$

The above results are valid for the case of a fully rough wall ($N = \sin \phi / \tan \delta = 1$). For smoother walls ($N > 1$), the outer solution is uniformly valid in the limit $\epsilon \rightarrow 0$.

REFERENCES

- [1] Jackson, R.: Some mathematical and physical aspects of continuum models for the motion of the granular materials. In: *Theory of Dispersed Multiphase Flow* (Meyer, R. E., ed.), pp. 291–337. New York: Academic Press (1983).
- [2] Roscoe, K. H.: The influence of strains in soil mechanics. 10th Rankine Lecture. *Géotechnique* **20**, 129–170 (1970).
- [3] Nedderman, R. M., Laohakul, C.: The thickness of shear zone of flowing granular materials. *Powder Technol.* **25**, 91–100 (1980).
- [4] Gudehus, G., Tejchman, J.: Some mechanisms of a granular mass in a silo-model tests and a numerical Cosserat approach. In: *Advances in Continuum Mechanics* (Brüller, O., Mannel, V., Najjar, J., eds.), pp. 178–194. Springer (1991).
- [5] Tejchman, J., Gudehus, G.: Silo-music and silo-quake experiments and a numerical Cosserat approach. *Powder Technol.* **76**, 201–212 (1993).
- [6] Tejchman, J., Wu, W.: Numerical study of patterning of shear bands in a Cosserat continuum. *Acta Mech.* **99**, 61–74 (1993).
- [7] Mohan, L. S., Nott, P. R., Rao, K. K.: Fully developed flow of coarse granular materials through a vertical channel. *Chem. Engng Sci.* **52**, 913–933 (1997).
- [8] Mühlhaus, H. B.: Shear band analysis in granular materials by Cosserat theory. *Ing. Archiv.* **56**, 389–399 (1986).
- [9] Mühlhaus, H. B., Vardoulakis, I.: The thickness of shear bands in granular materials. *Géotechnique* **37**, 271–283 (1987).
- [10] Lun, C. K. K., Savage, S. B., Jeffrey, D. J., Chepurniy, N.: Kinetic theories for granular flow: inelastic particles in Couette flow and slightly inelastic particles in a general flow field. *J. Fluid Mech.* **140**, 223–256 (1984).
- [11] Mühlhaus, H. B.: Application of cosserat theory in numerical solution of limit load problems. *Ing. Arch.* **59**, 124–137 (1989).
- [12] Tejchman, J., Wu, W.: Numerical study on sand and steel interfaces. *Mech. Res. Comm.* **21**, 109–119 (1994).
- [13] Jaunzemis, W.: *Continuum Mechanics*. New York: The Macmillan Company (1967).
- [14] Cowin, S. C.: The theory of polar fluids. *Adv. Appl. Mech.* **14**, 279–347 (1974).
- [15] Dahler, J. S.: Transport phenomena in a fluid composed of diatomic molecules. *J. Chem. Phys.* **30**, 1447–1475 (1959).

- [16] Campbell, C. S.: Boundary interaction for two-dimensional granular flows. Part 1. Flat boundaries, asymmetric stresses and couple stresses. *J. Fluid Mech.* **247**, 111–136 (1993).
- [17] Jenkins, J. T., Cundall, P. A., Ishibashi, I.: Micromechanical modeling of granular materials with the assistance of experiments and numerical simulations. In: *Powders and Grains* (Biarez, Gourvès, eds.), pp. 257–264. Netherlands: A. A. Balkema (1989).
- [18] Besdo, D.: Ein Beitrag zur nichtlinearen Theorie des Cosserat-Kontinuums. *Acta Mech.* **20**, 105–131 (1974).
- [19] Lippmann, H.: Cosserat plasticity and plastic spin. *Appl. Mech. Rev.* **48**, 753–762 (1995).
- [20] de Borst, R.: A generalisation of the J_2 -flow theory for polar continua. *Comp. Methods in Appl. Mech. and Engng* **103**, 347–362 (1993).
- [21] Schofield, A. N., Wroth, C. P.: *Critical State Soil Mechanics*. London: McGraw-Hill (1968).
- [22] Prakash, J. R., Rao, K. K.: Steady compressible flow of granular materials through a wedge-shaped hopper: the smooth wall radial gravity problem. *Chem. Engng Sci.* **43**, 479–494 (1988).
- [23] Johnson, P. C., Jackson, R.: Frictional-collisional constitutive relations for granular materials, with application to plane shearing. *J. Fluid Mech.* **176**, 67–93 (1987).
- [24] Brennen, C., Pearce, J. C.: Granular material flow in two dimensional hoppers. *ASME J. of Appl. Mech.* **45**, 43–50 (1978).
- [25] Nedderman, R. M.: *Statics and Kinematics of Granular Materials*. Cambridge: Cambridge University Press (1992).
- [26] Petzold, L.: Automatic selection of methods for solving stiff and nonstiff systems of ordinary differential equations. *SIAM J. Sci. Stat. Comput.* **4**, 136–148 (1983).
- [27] Natarajan, V. V. R., Hunt, M. L., Taylor, E. D.: Local measurements of velocity fluctuations and diffusion coefficients for a granular material flow. *J. Fluid Mech.* **304**, 1–25 (1995).
- [28] Tüzün, U., Nedderman, R. M.: Gravity flow of granular materials round obstacles—II. *Chem. Engng Sci.* **40**, 337–351 (1985).
- [29] Jyotsna, R., Rao, K. K.: Flow of coarse granular materials through a wedge-shaped hopper. *J. Fluid Mech.* **346**, 239–270 (1997).
- [30] Fickie, K. E., Mehrabi, R., Jackson, R.: Density variations in a granular material flowing from a wedge-shaped hopper. *AIChE. J.* **35**, 853–855 (1989).
- [31] Press, W. H., Teukolsky, S. A., Vetterling, W. T., Flannery, B. P.: *Numerical Recipes in Fortran*. Cambridge: Cambridge University Press (1992).
- [32] Kaza, K. R.: *The mechanics of flowing granular materials*. Ph.D. thesis, University of Houston (1982).
- [33] Dienes, J. K.: On the analysis of rotation and stress rate in deforming bodies. *Acta Mech.* **32**, 217–232 (1979).
- [34] Van Dyke, M.: *Perturbation Methods in Fluid Mechanics*. New York: Academic Press (1964).
- [35] Bender, C. M., Orszag, S. A.: *Advanced Mathematical Methods for Scientists and Engineers*. Singapore: McGraw Hill (1984).

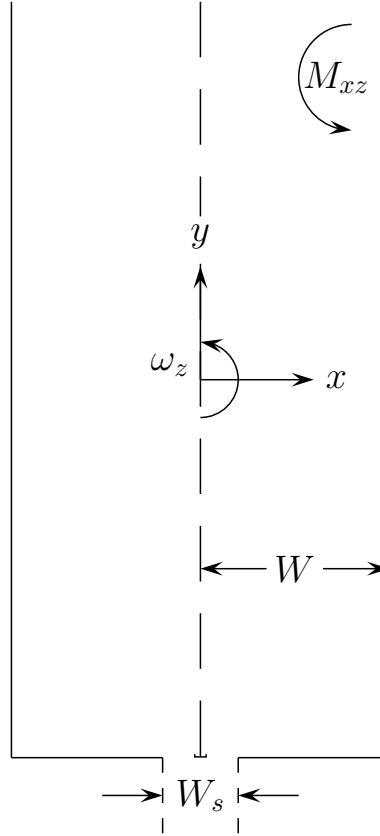


Fig. 1. Elevation of the channel. The angular velocity ω_z is positive for an anti-clockwise rotation about the z -axis. The couple stress M_{xz} exerted on the plane $x = \text{constant}$ by the material to the left of this plane is positive when the couple is directed as shown.

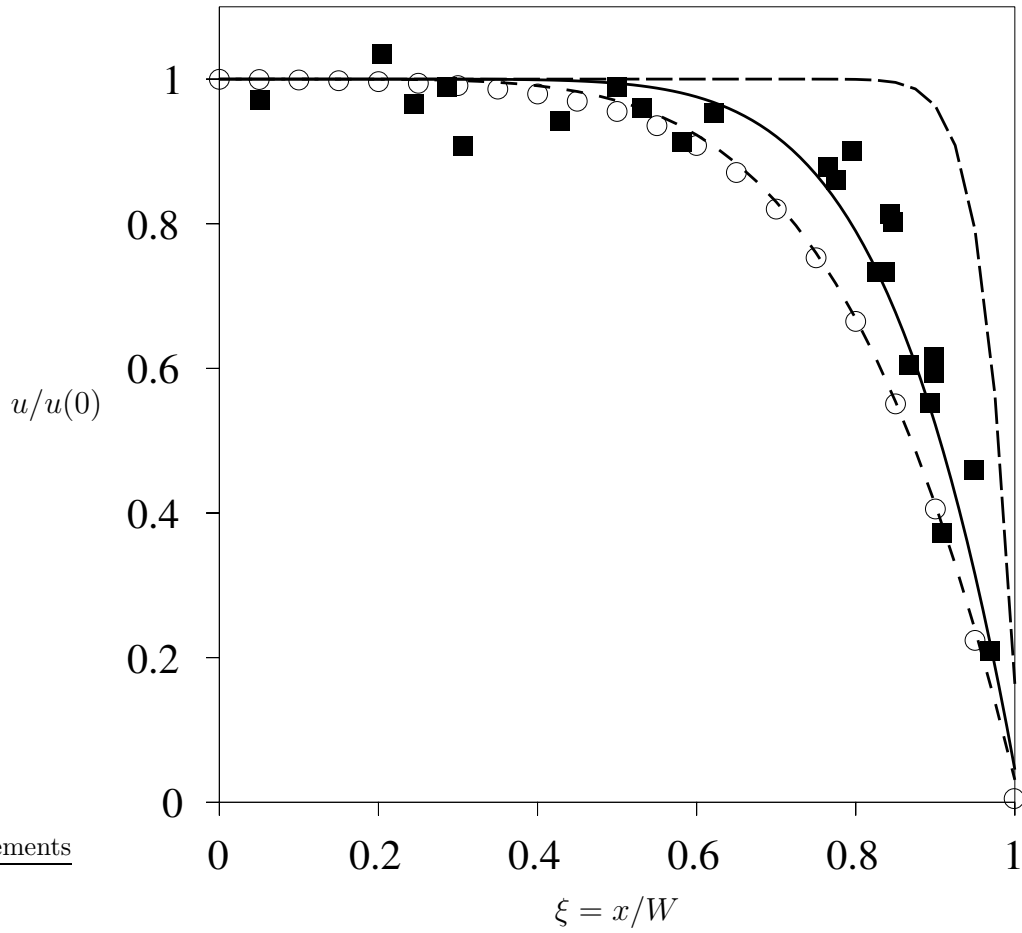


Fig. 2. Scaled velocity profiles: (○) asymptotic solution, (■) data of Nedderman and Laohakul [3] for glass beads. The curves represent numerical solutions with $L = 2$ (-----), 10 (————) and 20 (- · - · -). Parameter values: $A = 1/3$, $K = 0.5$, $W = 0.06$ m, $d_p = 0.002$ m, ($\epsilon = 1/30$), $u(\xi = 0) = 0.2$, $\rho_p = 2940$ kg/m³, and $\phi = 25^\circ$ ($\delta = 22.91^\circ$).

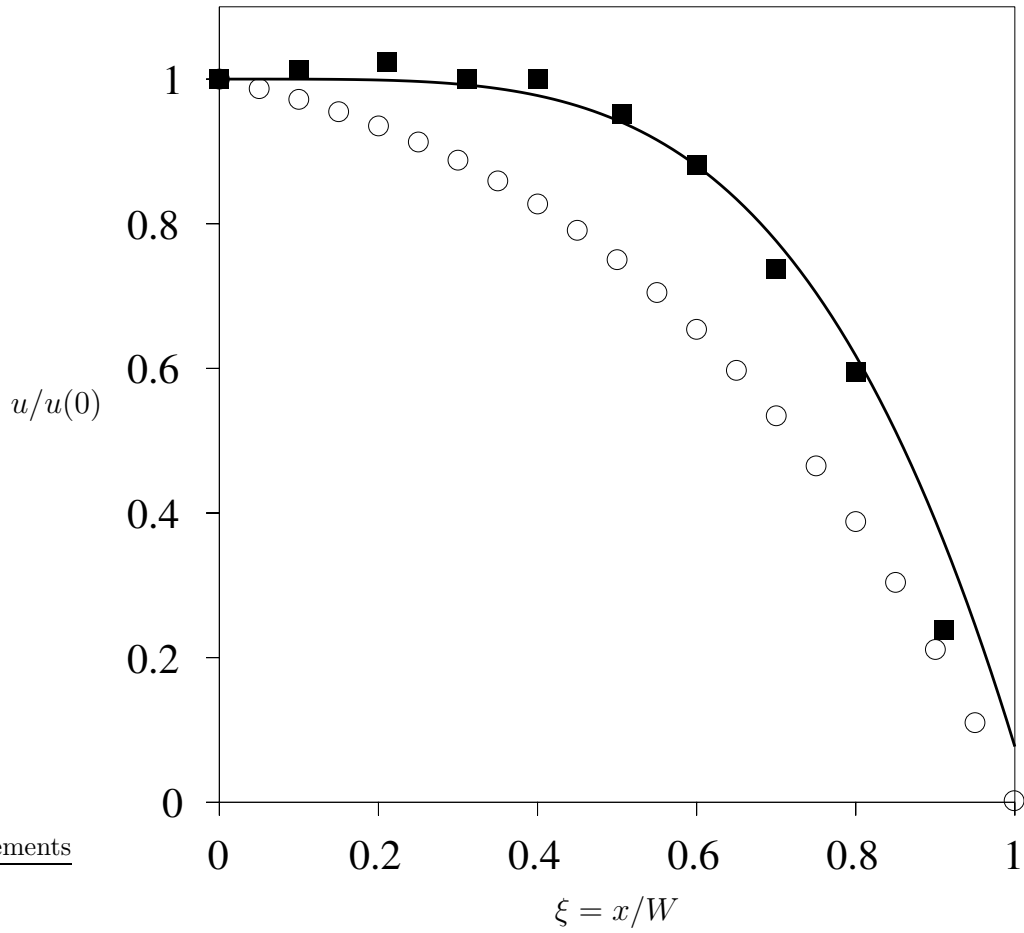


Fig. 3. Scaled velocity profiles: (—) numerical solution, (○) asymptotic solution (■) data of Natarajan *et al.* [27] for glass beads. Parameter values: $W = 0.0255$ m, $d_p = 0.003$ m, ($\epsilon = 0.12$), dimensionless mass flow rate $\int_0^1 u v d\xi = 0.15$, $\phi = 28^\circ$ ($\delta = 25.15^\circ$), $L = 10$, the rest as in figure 2.

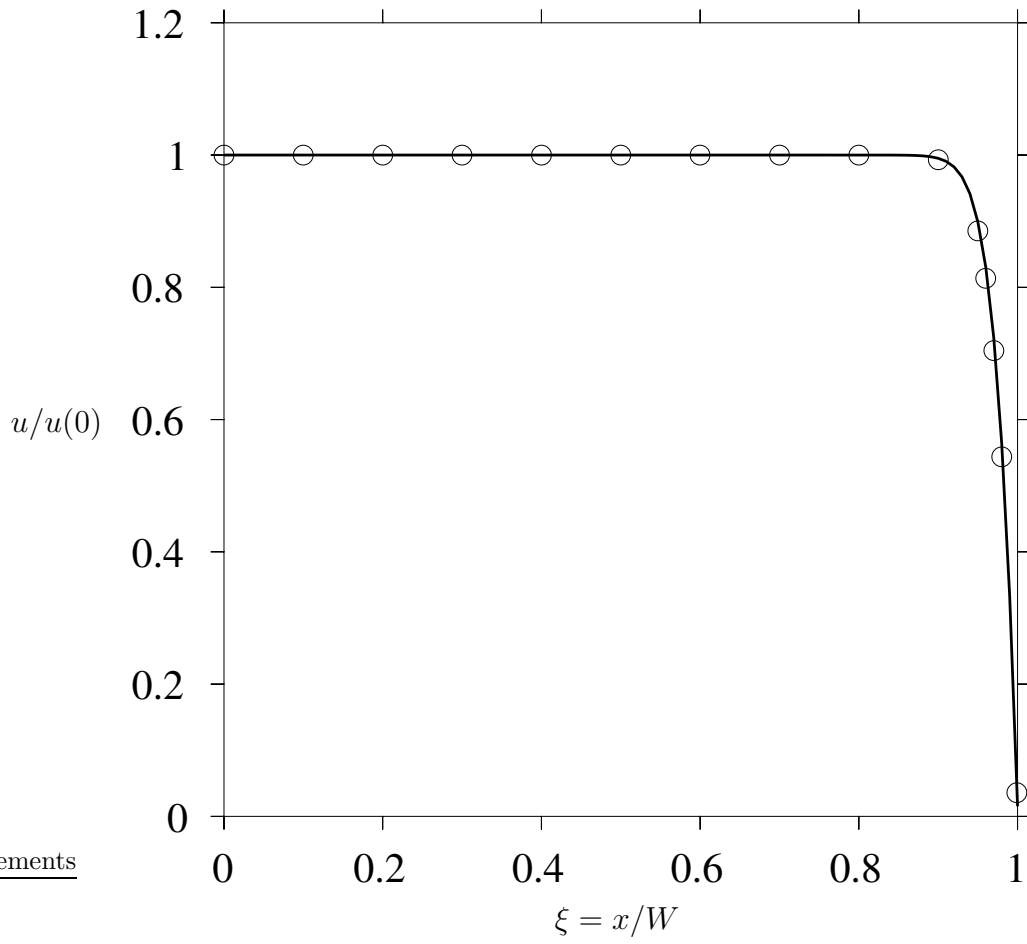


Fig. 4. Scaled velocity profiles: (—) numerical solution, (o) asymptotic solution. Parameter values: $W = 1.2$ m, ($\epsilon = 1/600$), $L = 10$, the rest as in figure 2.

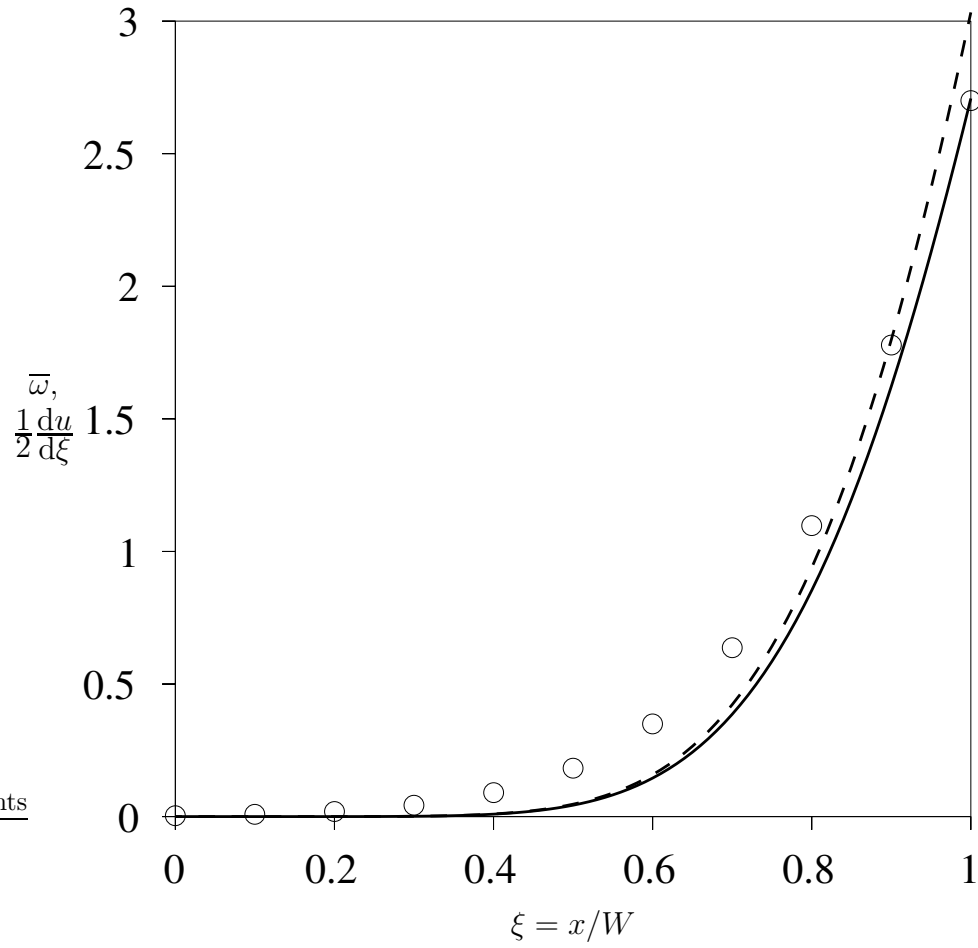


Fig. 5. Profiles of the angular velocity (—) $\bar{\omega}$, (---) half the dimensionless vorticity, $(1/2)du/d\xi$, and the asymptotic solution for $\bar{\omega}$ (\circ). Parameter values: $L = 10$, the rest as in figure 2.

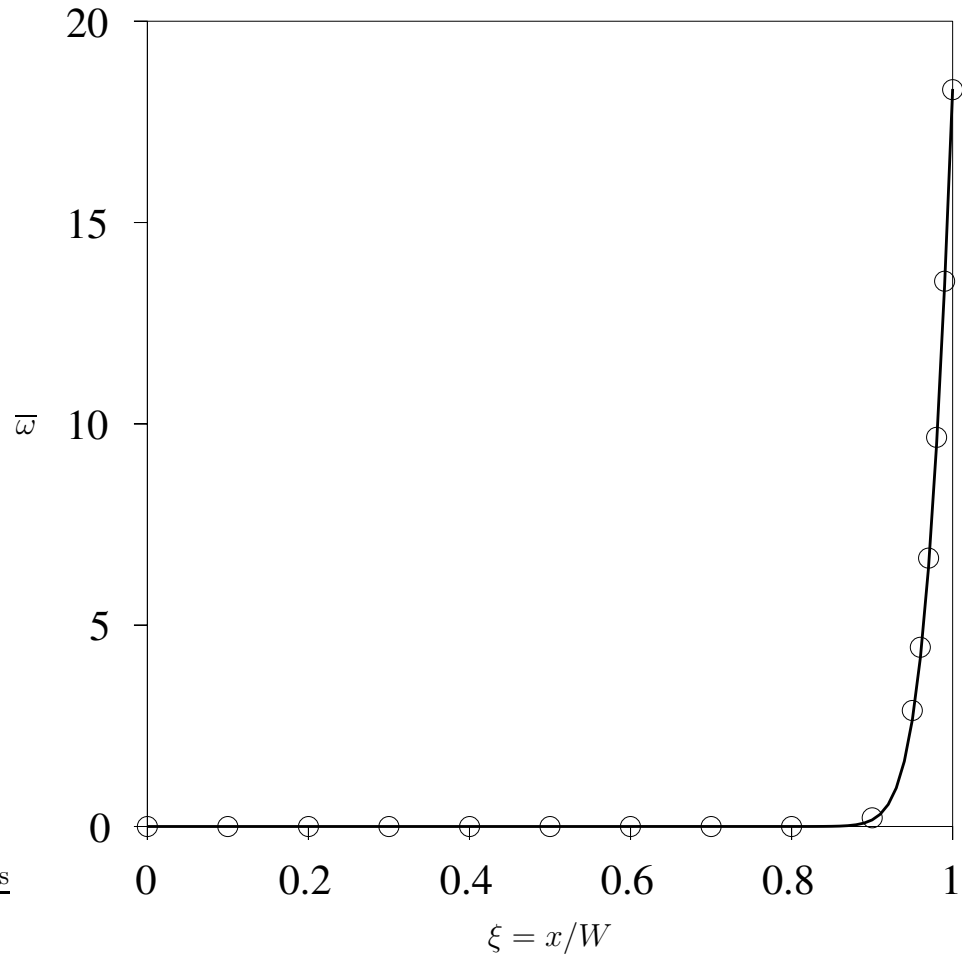


Fig. 6. Profiles of the angular velocity: (—) $\bar{\omega}$, and (o) the asymptotic solution for the angular velocity. Parameter values: $W = 1.2$ m, ($\epsilon = 1/600$), $L = 10$, the rest as in figure 2.

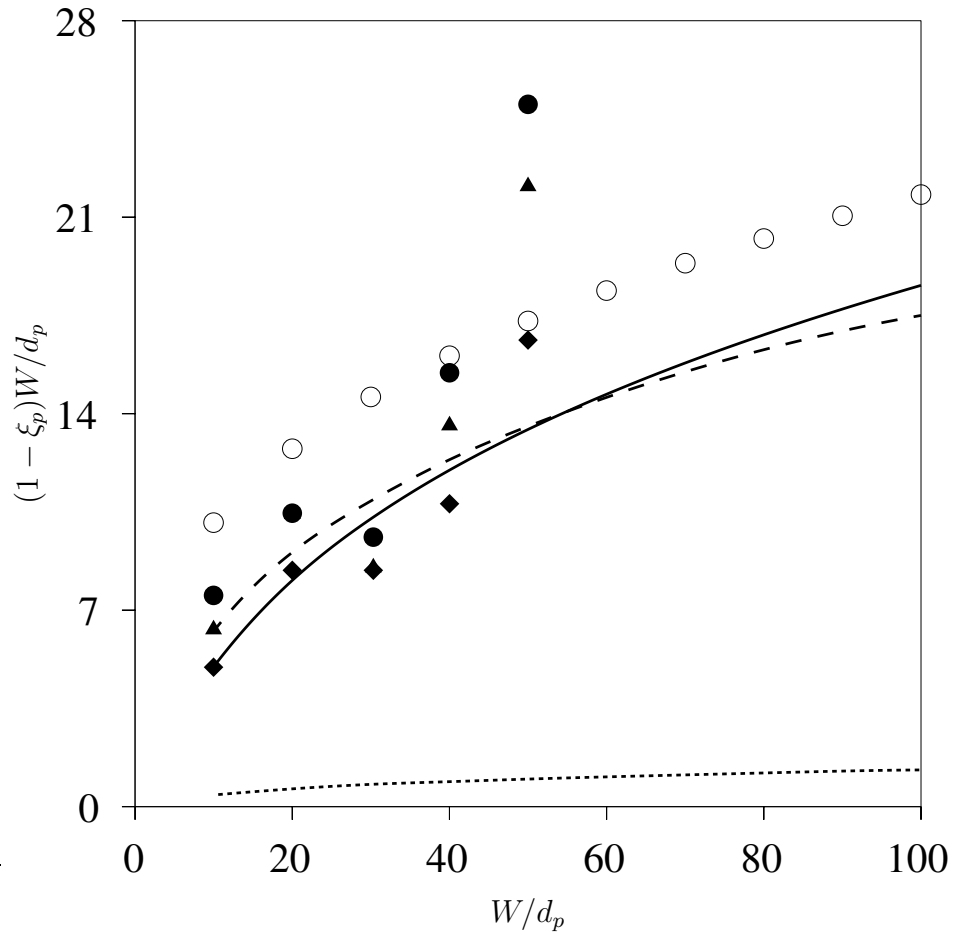


Fig. 7. Effect of the channel width $2W$ on the thickness of the shear layer (scaled by the particle diameter): (—) numerical solution, (o) asymptotic solution, (---) kinetic solution, and (.....) the frictional-kinetic solution. Here the solid symbols represent the estimates of Nedderman and Laohakul [3], obtained by fitting the data to three different functional forms. Parameter values: $L = 10$, the rest as in figure 2.

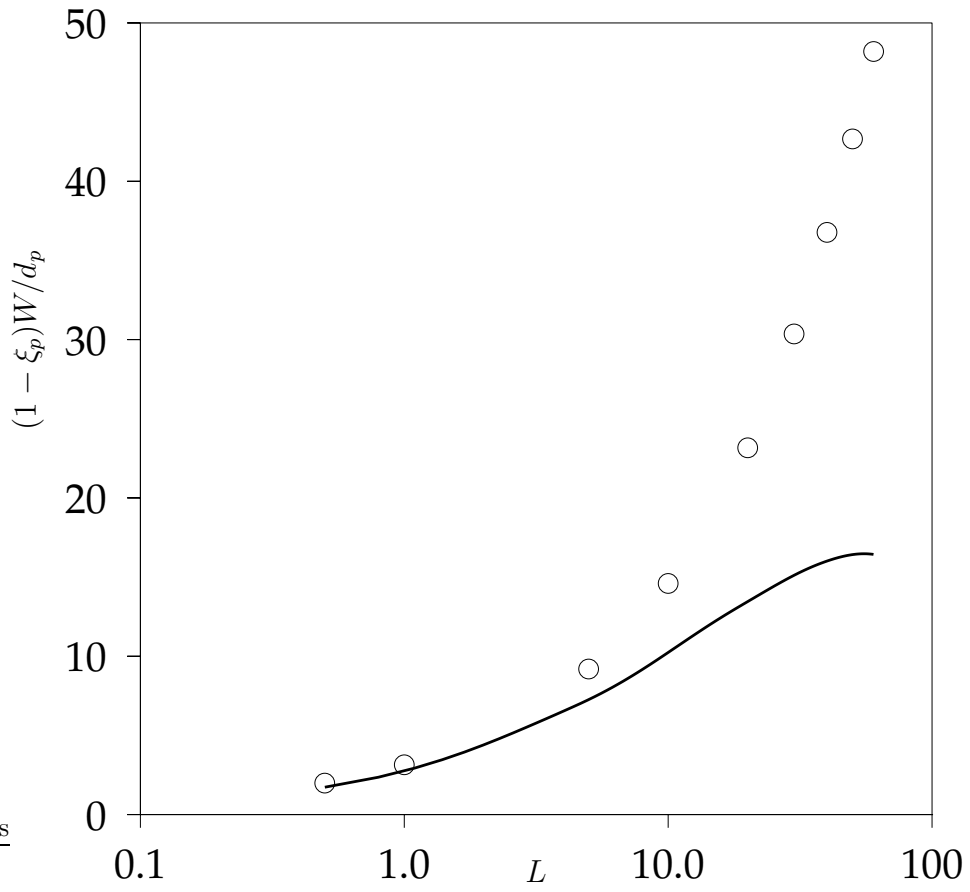


Fig. 8. Influence of L on the predicted thickness of the shear layer: (—) numerical solution, (○) asymptotic solution. Parameter values as in figure 2.

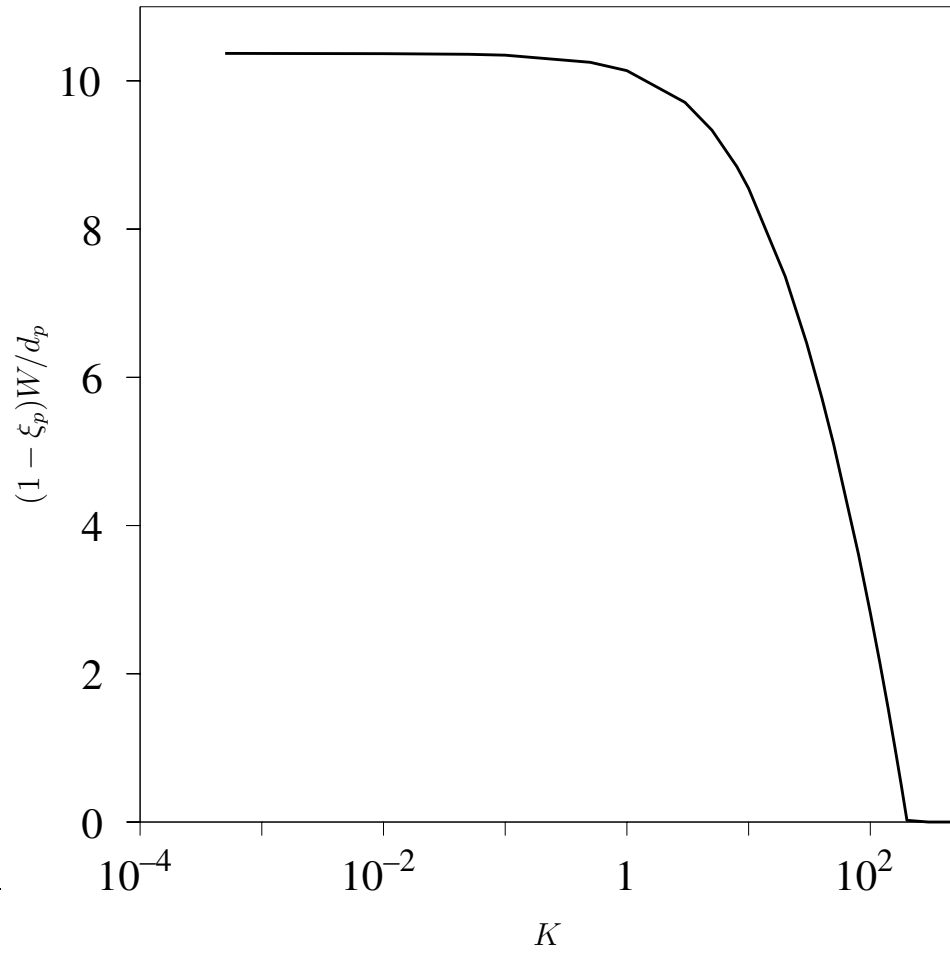


Fig. 9. Influence of K on the predicted thickness of the shear layer. Parameter values as in figure 2.

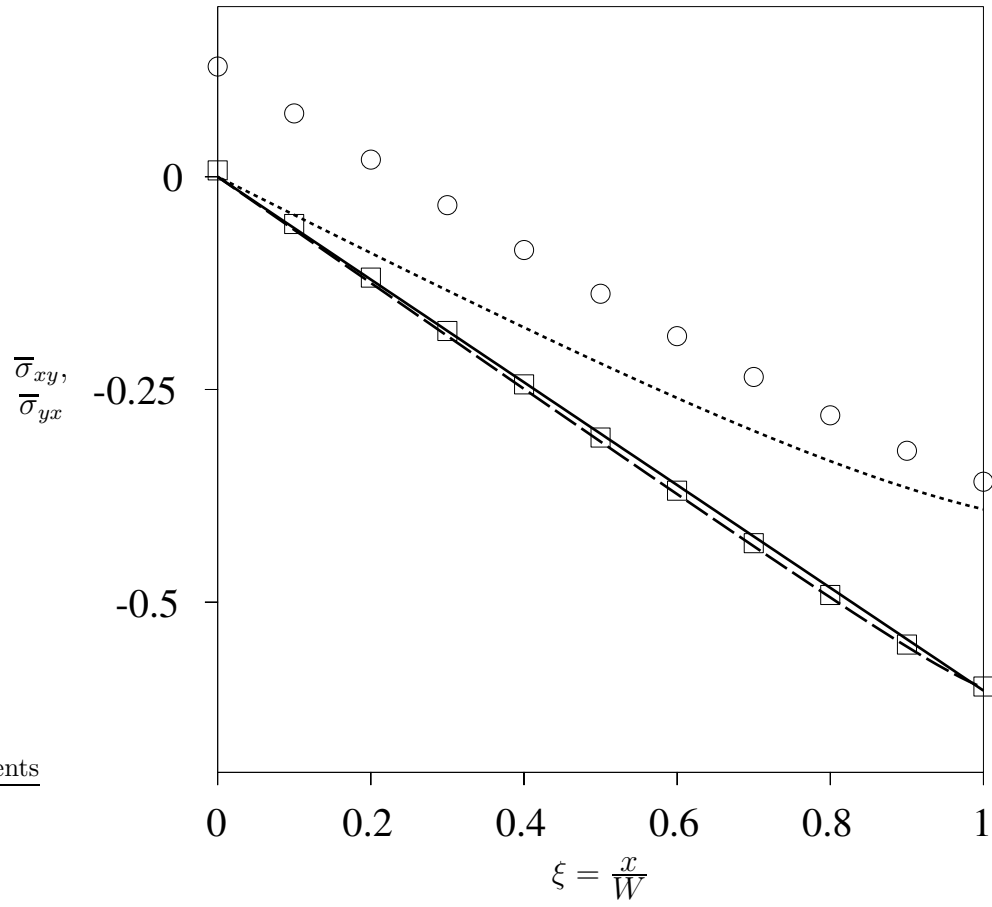


Fig. 10. Profiles of the shear stresses: (—) $\bar{\sigma}_{xy}$, $\bar{\sigma}_{yx}$ (....., $\epsilon = 1/30$; ---, $\epsilon = 1/600$). The symbols represent the asymptotic solutions for $\bar{\sigma}_{yx}$ (o, $\epsilon = 1/30$; □, $\epsilon = 1/600$). Parameter values: $L = 10$, the rest as in figure 2.

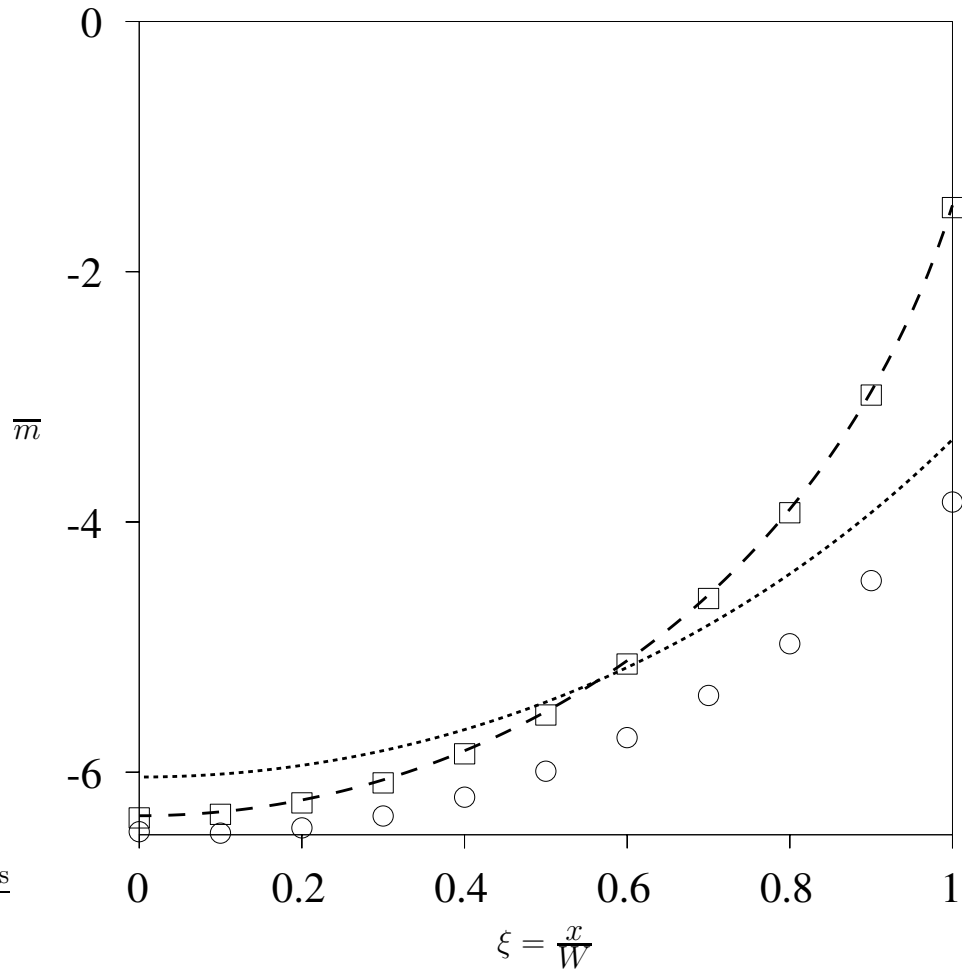


Fig. 11. Profiles of the couple stress \bar{m} (....., $\epsilon = 1/30$; -----, $\epsilon = 1/600$). The symbols represent asymptotic solutions (\circ , $\epsilon = 1/30$; \square , $\epsilon = 1/600$). Parameter values as in figure 2.

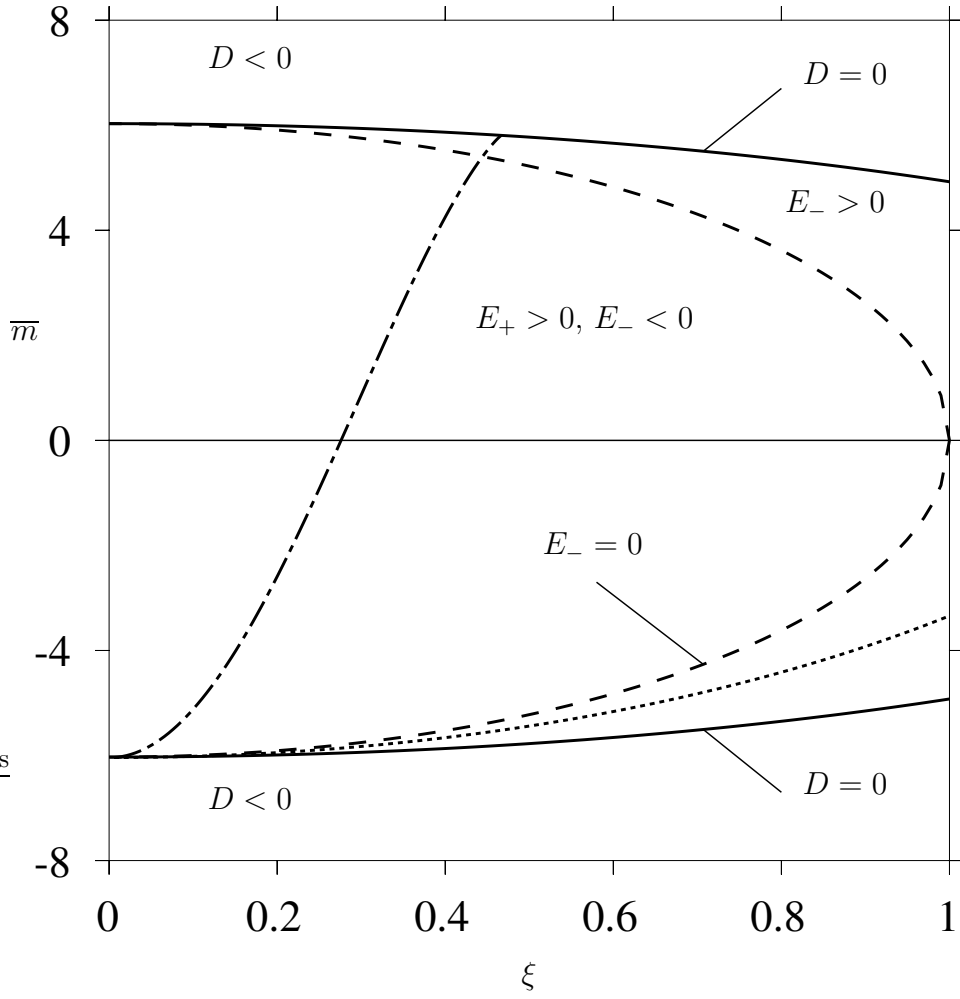


Fig. 12. Phase plane of the angular momentum balance equations (A1) and (A2): --- , trajectory corresponding to (A1); --- , trajectory corresponding to (A2). In both cases, the initial condition is $\bar{m}(0) = -NL\nu$. Parameter values: $N = 1$, $L = 10$, ($\nu = 0.603$), $A = 1/3$, $\epsilon = 1/30$.